Modeling RedOx-based magnetohydrodynamics in three-dimensional microfluidic channels

Hussameddine Kabbani, Aihua Wang, Xiaobing Luo, and Shizhi Qian

Citation: Physics of Fluids (1994-present) **19**, 083604 (2007); doi: 10.1063/1.2759532
View online: http://dx.doi.org/10.1063/1.2759532
View Table of Contents: http://scitation.aip.org/content/aip/journal/pof2/19/8?ver=pdfcov
Published by the AIP Publishing

Modeling RedOx-based magnetohydrodynamics in three-dimensional microfluidic channels

Hussameddine Kabbani and Aihua Wang
Department of Mechanical Engineering, University of Nevada Las Vegas, 4505 Maryland Parkway, Las Vegas, Nevada 89154-4027, USA

Xiaobing Luo
School of Energy and Power, Huazhong University of Science and Technology, Wuhan, China, 430074

Shizhi Qian[a)]
Department of Mechanical Engineering, University of Nevada Las Vegas, 4505 Maryland Parkway, Las Vegas, Nevada 89154-4027, USA

(Received 23 October 2006; accepted 13 June 2007; published online 30 August 2007)

RedOx-based magnetohydrodynamic (MHD) flows in three-dimensional microfluidic channels are investigated theoretically with a coupled mathematical model consisting of the Nernst-Planck equations for the concentrations of ionic species, the local electroneutrality condition for the electric potential, and the Navier-Stokes equations for the flow field. A potential difference is externally applied across two planar electrodes positioned along the opposing walls of a microchannel that is filled with a dilute RedOx electrolyte solution, and a Faradaic current transmitted through the solution results. The entire device is positioned under a magnetic field which can be provided by either a permanent magnet or an electromagnet. The interaction between the current density and the magnetic field induces Lorentz forces, which can be used to pump and/or stir fluids for microfluidic applications. The induced currents and flow rates in three-dimensional (3D) planar channels obtained from the full 3D model are compared with the experimental data obtained from the literature and those obtained from our previous two-dimensional mathematical model. A closed form approximation for the average velocity (flow rate) in 3D planar microchannels is derived and validated by comparing its predictions with the results obtained from the full 3D model and the experimental data obtained from the literature. The closed form approximation can be used to optimize the dimensions of the channel and to determine the magnitudes and polarities of the prescribed currents in MHD networks so as to achieve the desired flow patterns and flow rates.
 [DOI: 10.1063/1.2759532]

I. INTRODUCTION

Lab-on-a-chip (LOC) is a minute chemical processing plant, where common laboratory procedures ranging from filtration and mixing to separation and detection are done in the palm of the hand. This technology has the potential of revolutionizing various bioanalytical applications. The interconnected networks of microchannels and reservoirs with tiny volumes of reagents are well matched with the demands for small volume, low cost, rapid response, massive parallel analyses, automation, and minimal cross-contamination that characterize many applications in biotechnology. Fluid manipulation such as fluid propulsion and mixing is one of the central problems facing the designer of such LOC devices.

In recent years, various means for propelling the fluid in networks of microchannels have been proposed, such as pressure-driven flow, electrokinetically driven flow (electroosmosis, electrophoresis, and dielectrophoresis), surface tension driven flow, centrifugally driven flow, buoyancy-driven flow, and magnetohydrodynamics (MHD) flow, to quote only a few of them. Relative to other methods for manipulating fluids for various microfluidic applications, the MHD-based LOC devices can be operated at very low voltages and with no moving parts. In addition, MHD propulsion is one of the few methods that allow pumping of weakly conductive liquids such as buffer solutions along a closed loop, thereby forming a conduit with an "infinite length." Up to now, various MHD micropumps[1–13] and stirrers[14–19] operating under either AC or DC electric fields have been designed, modeled, constructed, and tested for various applications. The use of AC electric fields usually induces inductive eddy current with significant energy dissipation and heating. By using DC fields, the serious heating problems resulting from the induced eddy currents can be solved. However, two problems that have hindered the practical application of DC MHD microfluidics are short electrode lifetime and bubble generation due to electrolysis. The introduction of RedOx species into the liquid is a potential solution to the problems associated with the DC MHD microfluidics.[20–26] RedOx-based DC MHD has several benefits. For example, the electric potential applied across the electrodes can be very low (several mV to ~1 V), which eliminates the bubble generation problem. In addition, the electrode lifetime is longer because electrode

[a)]Author to whom correspondence should be addressed. Electronic mail: shizhi.qian@unlv.edu

oxidation does not occur in the presence of the electroactive RedOx species.

There are a large number of factors that affect the operation and performance of RedOx-based MHD devices: the concentrations of the electroactive and supporting electrolyte, the type of the RedOx species, the aspect ratio of the microchannel's cross section, the configuration of the electrodes, the externally applied electric potential or electric current, and the strength of the magnetic field. To achieve the desired flow rates and flow patterns in the RedOx-based MHD microfluidics, theoretical analysis of RedOx-based MHD flow in two-dimensional (2D) planar conduits has been conducted.[23] In the current study, we extend the theoretical analysis of 2D to three-dimensional (3D) microchannels, which are more close to the practical applications.

The rest of the paper is organized as follows. Section II introduces the mathematical model for the conjugate problem of MHD flow, electron transfer, and ionic mass transport of both electroactive and inert species. Section III describes the code validation by comparing our numerical predictions with a few special cases reported in the literature. Section IV provides the resulting current and flow rate as functions of the applied potential difference, bulk concentration of the RedOx electrolyte, and the magnetic flux density. When the electric currents instead of the potential differences are prescribed in 3D planar microconduits with rectangular cross sections, a closed form approximate model is derived. The results obtained from the models are compared with experimental data obtained from the literature. Section V concludes.

II. MATHEMATICAL MODEL

In this section, we introduce a full 3D mathematical model consisting of the Navier-Stokes equations for the fluid motion, the Nernst-Planck equations for the concentrations of both the electroactive and inert species, and the local electroneutrality condition for the electric potential in the electrolyte solution. This model accounts for the quasireversible oxidation and reduction reactions at the electrodes' surfaces and the convection induced by the Lorentz force through the interaction between the Faradaic current and the external magnetic field that can be provided by either a permanent magnet or an electromagnet.

Let us consider a planar microchannel with a rectangular cross section connecting two identical reservoirs on either side. In the current analysis, we neglect the effects of the two reservoirs on the fluid motion and the ionic mass transport within the microchannel. The length, width, and height of the microchannel are, respectively, L, W, and H. We use a Cartesian coordinate system with its origin positioned at one of the channel's corners. The coordinates x, y, and z are aligned, respectively, along the conduit's length, width, and depth ($0 \leqslant x \leqslant L$, $0 \leqslant y \leqslant W$, and $0 \leqslant z \leqslant H$). Two planar electrodes of length L_E and height H are deposited along the opposing walls with the leading edge located at a distance L_1 downstream of the conduit's entrance ($L_1 \leqslant x \leqslant L_1 + L_E$, $0 \leqslant z \leqslant H$, $y=0$ and W, respectively). The portions of the conduit's walls that are not coated with electrodes are made of dielectric material. Figure 1 schematically depicts the three-dimensional, planar microchannel with two electrodes deposited along the opposing walls. The conduit is filled with a dilute quasireversible RedOx electrolyte solution such as the mixture of $K_4[Fe(CN)_6]$ and $K_3[Fe(CN)_6]$. Different from our previous analysis of the 2D RedOx-based MHD flows in which the height of the channel is assumed to be much larger than its width (i.e., $H \gg W$), the current analysis has no assumption made concerning the aspect ratio H/W. Generally, MHD microfluidic devices have microchannels with a height of the same order of its width. Therefore, the current analysis is more close to the practical applications.

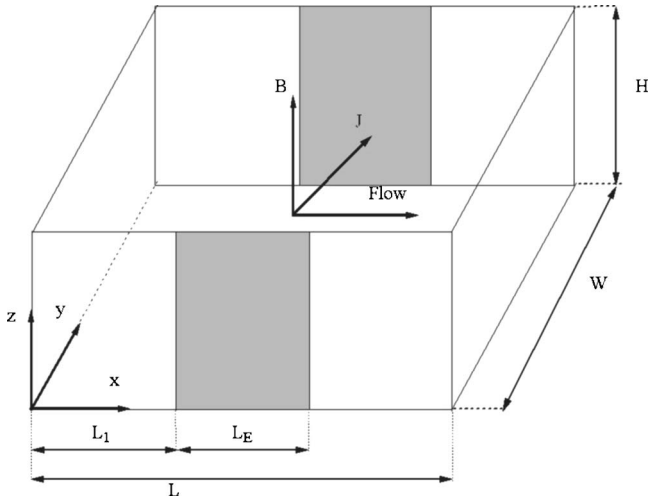

FIG. 1. Schematics of a three-dimensional, planar microchannel equipped with two electrodes positioned along the opposing walls. The channel is filled with a dilute RedOx electrolyte solution and subjected to a uniform magnetic flux density $\boldsymbol{B}$. A potential difference ΔV is applied across the electrodes resulting in a current density $\boldsymbol{J}$ transmits through the electrolyte solution. The interaction between the current density and the magnetic field induces Lorentz forces which pump the fluid from one end of the channel to the other.

When a potential difference, ΔV, is applied across the two electrodes deposited along the opposing walls, a current density $\boldsymbol{J}$ transmitted through the electrolyte solution results. Hereafter, bold letters denote vectors. We assume that the entire device is positioned under a magnetic field with a uniform magnetic flux density $\boldsymbol{B}=B\mathbf{e}_z$ directed in the z direction. Here, $\mathbf{e}_z$ is a unit vector in the z direction. The interaction between the current density $\boldsymbol{J}$ and the magnetic field $\boldsymbol{B}$ induces a Lorentz force of density $\mathbf{F}_L=\mathbf{J}\times\mathbf{B}=J_yB\mathbf{e}_x-J_xB\mathbf{e}_y+0\mathbf{e}_z$, which can be used to manipulate fluids. In the above expression, J_x and J_y are, respectively, the x and y component current densities; $\mathbf{e}_x$ and $\mathbf{e}_y$ are, respectively, the unit vectors in the x and y directions.

A. The mathematical model for the fluid motion

We assume that the electrolyte solution is incompressible. Under steady state, the flow driven by both the Lorentz force and the pressure gradient is described with the continuity and Navier-Stokes equations:

$$\nabla \cdot \mathbf{u} = 0 \tag{1}$$

and

$$\rho \mathbf{u} \cdot \nabla \mathbf{u} = -\nabla p + \mu \nabla^2 \mathbf{u} + \mathbf{F}_L. \tag{2}$$

In the above, p is the pressure; ρ and μ denote, respectively, the electrolyte solution's density and dynamic viscosity; $\mathbf{u}=u\mathbf{e}_x+v\mathbf{e}_y+w\mathbf{e}_z$ is the fluid's velocity in which u, v, and w are, respectively, the velocity components in the x, y, and z directions; and $\boldsymbol{F_L}$ is the induced Lorentz force in the electrolyte solution, $\mathbf{F}_L=\mathbf{J}\times\mathbf{B}=J_yB\mathbf{e}_x-J_xB\mathbf{e}_y+0\mathbf{e}_z$. In the current work, we neglect (i) the natural convection induced by the density variations due to the electrochemical reactions on the surfaces of the electrodes,[27] (ii) the paramagnetic forces induced by the concentration gradients of the paramagnetic species,[28] and (iii) the induced magnetic field due to small Reynolds numbers of the MHD flows in microchannels.

Witness that the equations (1) and (2) in both 2D and 3D are the same in the vector form, but the components of the equations in 3D are different from those in 2D. For example, the Navier-Stokes equations (2) have two component equations in 2D, one for the x-component velocity, and the other for the y-component velocity. However, the momentum equations (2) have three component equations for u, v, and w, respectively, in three-dimensional space. Except for the difference on the governing equations, the boundary conditions in 3D are also different from those in 2D. For example, the boundary conditions on the planes $z=0$ and $z=H$ are required in the 3D case. In contrast to the previous analysis of 2D RedOx-based MHD flows,[23] the current analysis focuses on 3D RedOx-based MHD flows.

In order to solve Eqs. (1) and (2), appropriate boundary conditions are required. A nonslip boundary condition is specified at the solid walls of the microchannel:

$$\mathbf{u}(x,0,z) = \mathbf{u}(x,W,z) = \mathbf{0}, \tag{3}$$

$$\mathbf{u}(x,y,0) = \mathbf{u}(x,y,H) = \mathbf{0}. \tag{4}$$

In other words, all the velocity components along the solid walls of the microchannel are zero. Normal pressure boundary conditions are used at the entrance ($x=0$) and exit ($x=L$) of the microchannel:

$$p(0,y,z) = P_1, \tag{5}$$

$$\mathbf{t} \cdot \mathbf{u}(0,y,z) = 0, \tag{6}$$

$$p(L,y,z) = P_2, \tag{7}$$

$$\mathbf{t} \cdot \mathbf{u}(L,y,z) = 0, \tag{8}$$

where $\mathbf{t}$ is the unit vector tangent to the planes $x=0$ in (6) and $x=L$ in (8). The externally applied pressure gradient is $\Delta p/L$ with $\Delta p=P_1-P_2$. In the absence of the externally applied pressure gradient across the microchannel, $P_1=P_2=0$.

To numerically solve the flow field from Eq. (1) and the set of the equations (2) subjected to the boundary conditions (3)–(8), the spatial distribution of the current density, $\mathbf{J}=J_x\mathbf{e}_x+J_y\mathbf{e}_y+J_z\mathbf{e}_z$, within the electrolyte solution is required, and is developed in the next section.

B. The model for multi-ion mass transport

In this section, we present a more general multi-ion mass transport model, which includes the Nernst-Planck equation for the concentration of each ionic species and the local electroneutrality condition for the electric potential in the solution. In comparison to the previous analysis in two-dimensional space in which the height of the channel is assumed to be much larger than its width (i.e., $H \gg W$) and the ionic mass transport phenomenon is predominantly two-dimensional, the effects of the bottom ($z=0$) and top ($z=H$) dielectric walls on the ionic mass transport are taken into account in the current 3D analysis.

We assume that the electrolyte solution contains K dissolved ionic species ($k=1,\ldots,K$). The flux density of each aqueous species due to convection, diffusion, and migration is given by

$$\mathbf{N}_k = \mathbf{u}c_k - D_k \nabla c_k - z_k m_k F c_k \nabla V, \quad k=1,\ldots,K. \tag{9}$$

In the above, c_k is the molar concentration; D_k is the diffusion coefficient; z_k is the valence; and m_k is the mobility of the kth ionic species. The fluid velocity $\mathbf{u}$ is determined from the model for the fluid motion described in Sec. II A; F is Faraday's constant ($F=96484.6$ C/mol); and V is the electric potential in the electrolyte solution. According to the Nernst-Einstein relation, the mobility of the kth ionic species is

$$m_k = \frac{D_k}{RT}, \quad k=1,\ldots,K, \tag{10}$$

with R the universal gas constant and T the absolute temperature of the electrolyte solution.

Under steady state, the concentration of each ionic species is governed by the following Nernst-Planck equation:

$$\nabla \cdot \mathbf{N}_k = \frac{\partial N_{kx}}{\partial x} + \frac{\partial N_{ky}}{\partial y} + \frac{\partial N_{kz}}{\partial z} = 0, \quad k=1,\ldots,K. \tag{11}$$

In the above, N_{kx}, N_{ky}, and N_{kz} are, respectively, the x, y, and z components of the flux density of the kth species. The set of the equations (11) consist of $(K+1)$ unknown variables: the concentrations of K ionic species and the electric potential V in the electrolyte solution. The local electroneutrality condition provides the $(K+1)$ equation:

$$\sum_{k=1}^{K} z_i c_i = 0. \tag{12}$$

In Eq. (12), we neglect the electrical double layers formed in the vicinity of the electrodes since the width of the microconduit is much larger than the thickness of the electrical double layer.

The current density $\boldsymbol{J}$ in the electrolyte solution due to convection, diffusion, and migration is given by

$$\mathbf{J} = F\sum_{k=1}^{K} z_k \mathbf{N}_k. \tag{13}$$

The Nernst-Planck equations (11) and the local electroneutrality condition (12) constitute a well-understood and widely accepted approximation for electrochemical transport phenomenon. In order to numerically solve them, appropriate

boundary conditions for the concentration of each ionic species and the electric potential in the electrolyte solution are required.

Since the walls of the microchannel are impervious to inert species (no electrochemical reactions occur for that species), the net ionic fluxes of the inert species such as the ions K^+ normal to the walls of the microchannel are zero:

$$\mathbf{n} \cdot \mathbf{N}_k = 0, \tag{14}$$

for the inert species k on all solid walls. In the above, $\mathbf{n}$ is the unit vector normal to the corresponding surface.

Similarly, the net flux densities of the electroactive species such as $[Fe(CN)_6]^{3-}$ and $[Fe(CN)_6]^{4-}$ normal to the dielectric walls where no electrochemical reactions occur are also zero:

$$\mathbf{n} \cdot \mathbf{N}_k = 0, \tag{15}$$

for the electroactive species k on dielectric walls. On the surface of the electrodes deposited along the opposing walls ($L_1 \leqslant x \leqslant L_1 + L_E$, $0 \leqslant z \leqslant H$, $y=0$ and W), oxidation and reduction reactions occur, respectively, at the surfaces of the anode and cathode:

$$\mathrm{Ox} + ne^- \Leftrightarrow \mathrm{Red}. \tag{16}$$

When the RedOx solution is a mixture of $K_4[Fe(CN)_6]$ and $K_3[Fe(CN)_6]$, the species Ox and Red in the above electrochemical reaction correspond, respectively, to the ions $[Fe(CN)_6]^{3-}$ and $[Fe(CN)_6]^{4-}$, and the number of electrons exchanged in the electrochemical reaction (16) is $n=1$. Usually, the Butler-Volmer equation is used to describe the kinetics of the electrochemical reaction:[29,30]

$$\mathbf{n} \cdot \mathbf{N}_{\mathrm{Red}} = -\mathbf{n} \cdot \mathbf{N}_{\mathrm{Ox}} = k_0 (c_{\mathrm{Ox}} e^{-(\alpha n F/RT)\eta} - c_{\mathrm{Red}} e^{(1-\alpha)(nF/RT)\eta}), \tag{17}$$

where c_{Ox} and c_{Red} are, respectively, the concentrations of the electroactive species Ox and Red that are involved in the electrochemical reaction (16) at the edge of the electric double layer; α is the charge transfer coefficient for the cathodic reaction, usually ranging from 0.0 to 1.0; n represents the number of electrons exchanged in the reaction; k_0 is the reaction rate constant; and

$$\eta = \begin{cases} (U_{\mathrm{an}} - V), & \text{along the surface of anode,} \\ (U_{\mathrm{ca}} - V), & \text{along the surface of cathode,} \end{cases} \tag{18}$$

where U_{an} and U_{ca} are, respectively, the externally imposed potential on the anode and cathode, and $\Delta V = U_{\mathrm{an}} - U_{\mathrm{ca}}$ represents the potential difference applied across the opposing electrodes. Notice that the first and second terms in the right-hand side of expression (17) represent, respectively, the forward and backward reaction rates which depend on the concentrations of the reactive species at the electrode's surface (i.e., c_{Ox} and c_{Red}) and on η, the electric potential drop across the electric double layer formed next to the electrode.

At the inlet cross section ($x=0$) of the microchannel, we assume that the concentration of each species is determined from the bulk concentration of the electrolyte solution in the left reservoir:

$$c_k(0,y,z) = c_{k0}, \quad k = 1, \ldots, K, \tag{19}$$

and obeys the electroneutrality condition $\Sigma_{k=1}^{K} z_k c_{k0} = 0$.

At the exit cross section of the microchannel ($x=L$), the transport of all species is dominated by the convective flux due to sufficiently large Péclet numbers in the MHD flows:[31]

$$\mathbf{n} \cdot \mathbf{N}_k = \mathbf{n} \cdot (c_k \mathbf{u}), \quad k = 1, \ldots, K. \tag{20}$$

Similarly, appropriate boundary conditions for the electric potential are also required prior to solving the coupled partial differential equations (11) and the algebraic equation (12). At the inlet and exit cross sections of the microchannel, we assume that the x component electric field is zero:

$$\mathbf{n} \cdot \nabla V(0,y,z) = \mathbf{n} \cdot \nabla V(L,y,z) = 0. \tag{21}$$

Along the dielectric walls of the channel, the electric fields normal to the walls are zero:

$$\mathbf{n} \cdot \nabla V(x,y,z) = 0. \tag{22}$$

Along the surfaces of the electrodes, note that the potentials of the electrolyte immediately adjacent to the electric double layers are different from the potentials applied on the anode and cathode, and there is a potential drop across the electric double layer. Using expressions (13), (17), and (18), the potentials of the electrolyte at the edge of the electric double layers adjacent to the anode and cathode can be implicitly calculated from

$$\mathbf{n} \cdot \mathbf{J} = nFk_0 (c_{\mathrm{Ox}} e^{-(\alpha n F/RT)\eta} - c_{\mathrm{Red}} e^{(1-\alpha)(nF/RT)\eta}). \tag{23}$$

Witness that the models for the fluid motion and the ionic mass transport are strongly coupled. The flow field affects the mass transport due to the contribution of the convective flux in expression (9). On the other hand, the ionic mass transport affects the current density $\boldsymbol{J}$, which, in turn, affects the flow field through the Lorentz force $\mathbf{J} \times \mathbf{B}$. Therefore, one has to simultaneously solve the full 3D mathematical model which consists of the continuity and Navier-Stokes equations (1) and (2), the set of the Nernst-Planck equations (11), and the local electroneutrality condition (12) for the flow field, the ionic species' concentrations, and the potential of the electrolyte solution.

III. SOLVER VALIDATION

To numerically solve the strongly coupled three-dimensional system, we used the commercial finite element package COMSOL (version 3.3, www.femlab.com) operating with a 64 bit dual-processor workstation of 32 GB RAM (www.polywell.com). The 3D computational domain was discretized into quadratic triangular elements. We employed nonuniform elements with a larger number of elements next to the inlet and outlet cross sections, as well as along the surfaces of the electrodes where the electrochemical reactions occur. We compared the solutions obtained for different mesh sizes to ensure that the numerical solutions are convergent, independent of the size of the finite elements, and satisfy the various conservation laws. To verify the code, we compared the numerical predictions with solutions available in the literature for special cases such as an electrochemical reactor with known flow field and the two-dimensional

RedOx-based MHD flow in the presence of abundant supporting electrolyte under limiting current conditions.

We simulated the 2D parallel-plate electrochemical reactor (PPER) described in Georgiadou.[32] The PPER geometry is similar to the configuration depicted in Fig. 1 when $H \gg W$. The computational domain consists of an upstream region, a downstream region, and the region between two parallel electrodes positioned along the opposing walls (Fig. 1). In contrast to the MHD problem, in the PPER reactor, a parabolic flow field is specified. In other words, one only needs to solve the Nernst-Planck equations (11) using the prescribed velocity profile and Eq. (12). Our results are in excellent agreement with the finite difference results of Georgiadou.[32]

Recently, we derived an analytical solution of the 2D RedOx-based MHD flow in the presence of abundant supporting electrolyte under the limiting current conditions using the boundary layer theory.[23] Our numerical solution favorably agrees with the analytical solution mentioned above (results are not shown here).

We also solved the full mathematical model with the commercial computational fluid dynamics software FLUENT (www.Fluent.com) using the finite volume method and the obtained results favorably agree with those obtained from the software COMSOL using the finite element method (results are not shown here). The good agreement of our computational results with the results obtained with different computational techniques as well as other comparisons with specialized solutions for the RedOx-based MHD flow give us confidence in our computational results.

IV. RESULTS AND DISCUSSION

We first simulated the RedOx-based MHD flow in a 3D planar microchannel of 18 mm in length, 330 μm in width, and 670 μm in depth. The aspect ratio H/W is about 2, under which the 2D approximation is not appropriate and we have to model the flow field and mass transport in 3D. The electrodes cover the entire side walls of the microchannel (i.e., $L_1=0$, and $L_E=L$. The RedOx electrolyte solution is a mixture of $K_4[Fe(CN)_6]$ and $K_3[Fe(CN)_6]$ in the absence of a supporting electrolyte. The simulation conditions are the same as those used in the experiments conducted by Aguilar *et al.*[25] The electrolyte solution contains three ionic species K^+, $Fe(CN)_6^{3-}$, and $Fe(CN)_6^{4-}$ with charges $z_1=1$, $z_2=-3$, and $z_3=-4$, respectively. The diffusion coefficients at room temperature of the species K^+, $Fe(CN)_6^{3-}$, and $Fe(CN)_6^{4-}$ are, respectively, $1.957\times10^{-9}m^2/s$, $0.896\times10^{-9}m^2/s$, and $0.735\times10^{-9}m^2/s$.[33] For the electrochemical reaction, $Fe(CN)_6^{3-}+e^- \Leftrightarrow Fe(CN)_6^{4-}$, the reaction rate constant and the charge transfer coefficient are, respectively, $k_0 \approx 1.0\times10^{-3}$ m/s and $\alpha \approx 0.5$.[34] Since the ferricyanide and ferrocyanide system has a very high reaction rate constant, the obtained results are not sensitive to the values of k_0 and α. Since the RedOx electrolyte solution is very dilute, the density and dynamic viscosity of the RedOx electrolyte solution are assumed to be the same as those of water ($\rho \sim 1000$ kg/m^3 and $\mu \sim 10^{-3}$ Pa s). In all our computations, the temperature $T=298$ K, and the bulk concentrations of both $K_4[Fe(CN)_6]$ and $K_3[Fe(CN)_6]$ in the left reservoir are taken to be equal. We also assume that there is no externally applied pressure difference between the conduit's inlet and exit (i.e., $P_1=P_2$).

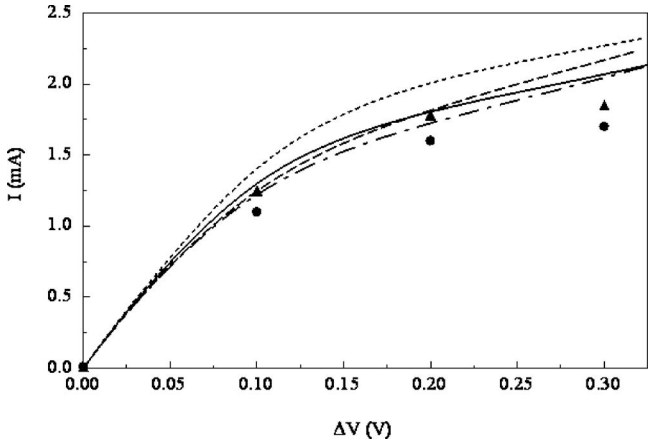

FIG. 2. The resulting current as a function of the applied potential difference in the presence ($B=0.44$ T) and absence ($B=0$) of a magnetic field. The symbols represent the experimental data obtained from the literature. The solid and dash-dotted lines represent, respectively, the resulting currents obtained from the full 3D model when $B=0.44$ T and $B=0$. The dotted and dashed lines represent, respectively, the currents obtained from the 2D model when $B=0.44$ T and $B=0$. The concentration of the RedOx species $K_4[Fe(CN)_6]/K_3[Fe(CN)_6]$, $C_0=0.25$ M, $L=18$ mm, $W=330$ μm, and $H=670$ μm.

The steady flow field and ionic concentration field under various potential differences (ΔV), bulk concentrations of the RedOx couple in the left reservoir (C_0), and magnetic flux densities (B) are obtained by simultaneously solving the coupled full 3D mathematical model described in Sec. II. Here we present the results of our numerical computations and compare them with the experimental data obtained by Aguilar *et al.*[25] Figure 2 depicts the steady-state current transmitted through the electrolyte solution as a function of the externally applied potential difference ΔV across the electrodes in the absence ($B=0$) and presence ($B=0.44$ T) of a magnetic field when the inlet bulk concentrations of $K_4[Fe(CN)_6]$ and $K_3[Fe(CN)_6]$ are $C_0=0.25$ M. In other words, the effects of the magnetic field on the resulting current are studied for two different magnetic flux densities, one at $B=0$ and the other at $B=0.44$ T under different potential differences. The circles (●) and triangles (▲) represent, respectively, the experimental data obtained from Aguilar *et al.*[25] for $B=0$ and $B=0.44$ T. The dash-dotted and solid lines in Fig. 2 represent, respectively, the currents obtained from the 3D model at $B=0$ and $B=0.44$ T. The dashed and dotted lines represent, respectively, the predicted currents from the 2D model at $B=0$ and $B=0.44$ T with the assumption of $H \gg W$. The current nonlinearly increases with the applied potential difference, and the theoretical predictions of the 3D model qualitatively agree with the experimental data. The discrepancies between the theoretical predictions and the experimental data may be due to the differences between the actual and assumed diffusion coefficients of the electroactive species. In the presence of a magnetic field, the interaction between the current density and the magnetic field induces a Lorenz force which pumps the fluid from the

reservoir located at the left end ($x=0$) to the reservoir positioned at the right end ($x=L$) of the channel. The induced fluid motion reduces the thicknesses of the concentration boundary layers formed next to the surfaces of the electrodes which, in turn, leads to an increase in the concentration gradient and current density along the surfaces of the electrodes. Consequently, the total current in the presence of a magnetic field is higher than that in the absence of a magnetic field in which there is no fluid motion. However, the effects of the magnetic field on the resulting current are not very significant under the above conditions. As expected, the currents obtained from the 2D model are higher than those obtained from the 3D model since the effects of the boundaries $z=0$ and $z=H$ on the fluid motion and the ionic mass transport are neglected in the 2D case. The 2D approximation is valid only when the aspect ratio $H/W \gg 1$, and is not appropriate for the experimental microchannel with the aspect ratio $H/W \approx 2$. Comparing to the resulting currents obtained from the 2D model, the currents obtained from the 3D model are closer to the experimental data.

In most regions of the planar microchannel, the current density $\boldsymbol{J}$ is directed nearly normal to the electrodes' surfaces, and the induced Lorentz force $\mathbf{J}\times\mathbf{B}$ is thus directed along the x direction. Consequently, the velocity components in the y and z directions are at least two orders of magnitude lower than the velocity component in the x direction. The x component velocity is nearly independent of the coordinate x, and its profile looks like a paraboloid (results are not shown here). Since the induced Lorentz force is a body force, the induced MHD flow is similar to a fully developed pressure-driven flow in a three-dimensional microchannel. The x-component velocity can be approximated with that of a fully developed duct flow with a rectangular cross section:[35]

$$u(y,z) = \frac{48\bar{U}}{\pi^3\left[1-\frac{192a}{\pi^5 b}\sum_{j=1,3,5,\ldots}^{\infty}\frac{\tanh(j\pi b/2a)}{j^5}\right]} \times \sum_{i=1,3,5,\ldots}^{\infty}(-1)^{(i-1)/2} \times\left[1-\frac{\cosh\left(\frac{i\pi(z-b)}{2a}\right)}{\cosh\left(\frac{i\pi b}{2a}\right)}\right]\frac{\cos\left(\frac{i\pi(y-a)}{2a}\right)}{i^3}, \tag{24}$$

where $a=W/2$, $b=H/2$, and $\bar{U}$ is the average velocity. The above approximation of the MHD flow with a fully developed pressure-driven Poiseuille flow has been used by many groups over years.[4,6,13,26] By substituting the velocity profile (24) into the x-component momentum equation and integrating that equation in the entire domain, the average velocity (flow rate) in terms of a series form can be obtained.[4,6,13,26] However, the obtained expression for the average velocity (flow rate) in terms of a series solution is not always practical for applications such as the inverse problems including the optimization of the channel's dimensions and the determination of the currents or voltages needed to achieve the desired flow rates and flow patterns in MHD microfluidic networks.[5,6] Therefore, we derive a closed form approximation for the average velocity (flow rate) which will be useful for solving the inverse problems in MHD networks.

The velocity profile (24) can be approximated with the following closed form approximation with an error less than 1%:[36]

$$u(y,z) = \bar{U}\left(\frac{m+1}{m}\right)\left(\frac{n+1}{n}\right)\left[1-\left(\frac{|y-a|}{a}\right)^n\right] \times\left[1-\left(\frac{|z-b|}{b}\right)^m\right], \tag{25}$$

with

$$m = 1.7 + 0.5\left(\frac{b}{a}\right)^{-1.4} \quad \text{and} \qquad n = \begin{cases} 2, & \text{for } \dfrac{b}{a} \leqslant \dfrac{1}{3}, \\ 2+0.3\left(\dfrac{b}{a}-\dfrac{1}{3}\right), & \text{for } \dfrac{b}{a} \geqslant \dfrac{1}{3}. \end{cases} \tag{26}$$

The steady x-component momentum equation can be approximated by

$$-\frac{\partial p}{\partial x} + \mu\left(\frac{\partial^2 u}{\partial y^2}+\frac{\partial^2 u}{\partial z^2}\right) + J_y B = 0. \tag{27}$$

Equation (27) represents a balance between the pressure force, the viscous force, and the Lorentz force. Substituting (25) into (27), and taking volume integration of Eq. (27), the average velocity becomes

$$\bar{U} = \frac{BIH-(P_2-P_1)H^2}{4\mu L\left[(n+1)\frac{H^2}{W^2}+(m+1)\right]} = G_1 I + G_2 \Delta p. \tag{28}$$

In the above, $\Delta p = P_1 - P_2$; $G_1 = \partial\bar{U}/\partial I$ and $G_2 = \partial\bar{U}/\partial\Delta p$ are, respectively, the electrical and hydraulic transport coefficients. As compared to the expression for the average velocity (flow rate) in terms of a series solution, the obtained closed form approximation (28) will be more practical to compute the flow rates in MHD networks and to solve the control (inverse) problem of determining the magnitudes and polarities of the applied currents of individually controlled branches in the MHD networks so as to achieve the desired flow patterns and flow rates.[5,6] In the absence of the pressure difference between the conduit's inlet and exit (i.e., $P_1 = P_2$), the average velocity is

$$\bar{U} = \frac{BIH}{4\mu L\left[(n+1)\frac{H^2}{W^2}+(m+1)\right]} = G_1 I. \tag{29}$$

Using the predefined velocity profile (25) instead of the series solution (24), one can easily simplify the coupled full mathematical model without solving the continuity and Navier-Stokes equations. In the 3D approximation model,

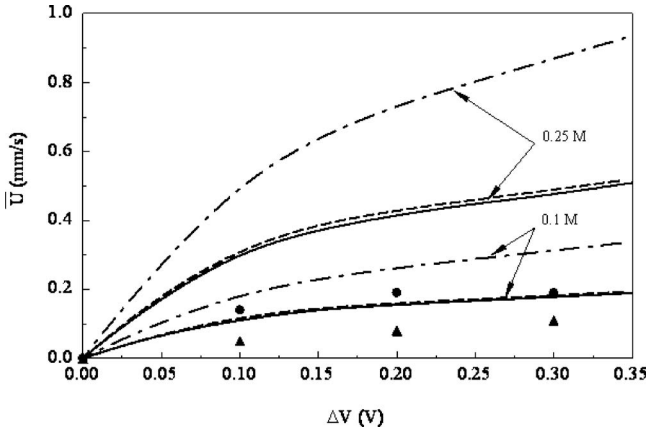

FIG. 3. The average velocity as a function of the applied potential difference for concentrations of the RedOx species $K_4[Fe(CN)_6]/K_3[Fe(CN)_6]$, C_0=0.1 and 0.25 M when B=0.44 T. The solid, dash-dotted, and dashed lines represent, respectively, the results obtained from the full 3D model, the full 2D model, and the 3D approximation model using the predefined velocity profile. The triangles and circles represent the experimental data obtained from the literature for C_0=0.1 and 0.25 M, respectively. All other conditions are the same as Fig. 2.

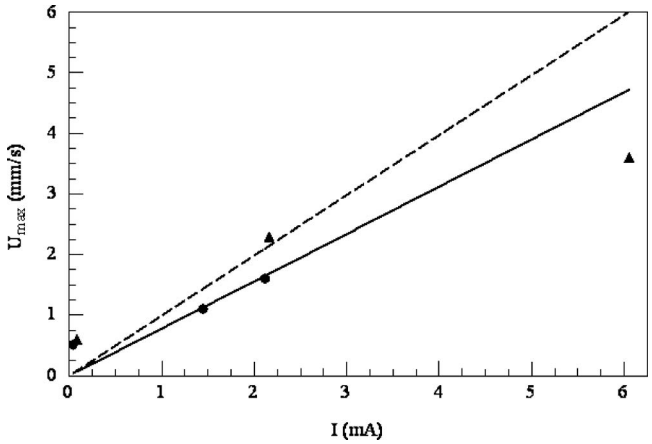

FIG. 4. The maximum velocity as a function of the current for the RedOx nitrobenzene with concentrations C_0=0.1 M (dashed line and circles) and C_0=0.25 M (solid line and triangles) when B=0.41 T, L=18 mm, W=270 μm, and H=640 μm. The lines and symbols represent, respectively, the predictions of the closed form approximation and the experimental data obtained from the literature.

one only needs to solve the mass transport equations (11) and (12) to determine the concentration field and the current density. Subsequently, the total current I can be obtained by integrating the current density along the surface of the anode. The average velocity and velocity profile can then be obtained from the expressions (28) and (25), respectively.

Next, we compare the average velocities obtained from the 2D model, the full 3D model, and the 3D approximation model with the experimental data obtained from the literature. Figure 3 depicts the average velocity $\bar{U}$ as a function of the applied potential difference for various bulk concentrations of the RedOx electrolyte when B=0.44 T. The triangles (▲) and circles (●) represent the experimental data obtained from Aguilar *et al.*[25] for the RedOx concentrations C_0=0.1 M and C_0=0.25 M, respectively. The solid, dashed, and dash-dotted lines in Fig. 3 represent, respectively, the predictions obtained from the full 3D mathematical model, the 3D approximation model using the velocity profile (25) and the expression (28), and the full 2D mathematical model. The predictions obtained from the full 3D mathematical model (solid lines) and from the 3D approximation model (dashed lines) are in good agreement. The average velocity increases nonlinearly with the potential difference. This behavior is attributed to the nonlinear relationship between the current and the applied potential difference as depicted in Fig. 2 since the average velocity is proportional to the current as shown in the closed form approximation (29). The predictions obtained from the full 3D mathematical model and from the 3D approximation model overpredict the experimental data, especially for the case with a higher bulk concentration (C_0=0.25 M). The experiments were conducted by tracing a dye placed on one end of the channel (i.e., x=0) which then was observed on the other end of the channel (i.e., x=L) after a certain time interval Δt. The average velocity is estimated as the ratio $L/\Delta t$. We would suspect that the measured velocities would appear to be slower than they really are because the dye can be seen on the exit reservoir only when its concentration is sufficiently high enough. The average velocities obtained from the 2D model (dash-dotted lines) are higher than those obtained from the 3D models due to the neglect of the boundary effects arising from the bottom (z=0) and top (z=H) walls in the 2D case. As compared to the deviations between the experimental data and the average velocities obtained from the 3D model, larger deviations between the experimental data and the average velocities predicted from the 2D model are obtained.

The closed form approximation is validated by comparing its predictions with the experimental data obtained from the literature. Figure 4 depicts the maximum velocity, U_{max}, as a function of the current for C_0=0.1 M (dashed line and circles) and 0.25 M (solid line and triangles) nitrobenzene (NB) species in a planar conduit of 18 mm in length, 270 μm in width, and 640 μm in height when the magnetic flux density B=0.41 T. Using the measured currents from the experiments, we estimated the average velocity $\bar{U}$ with the closed form approximation (29) in the absence of the externally applied pressure gradient. According to the expression (25), the maximum velocity is $U_{max}=[(m+1)(n+1)/mn]\bar{U}$. The lines and symbols in Fig. 4 represent, respectively, the predictions of the closed form approximation (29) and the experimental data obtained from Arumugam *et al.*[26] The predictions qualitatively agree with the experimental observations. The deviation between the solid and dashed lines is basically due to the difference in the dynamic viscosities of 0.1 and 0.25 M NB RedOx electrolyte solution. The dynamic viscosities for C_0=0.1 and 0.25 M NB electrolyte solution are, respectively, 0.000 38 and 0.000 43 Pa s,[26] which explains why the slope for C_0=0.25 M NB solution is smaller than that of C_0=0.1 M NB electrolyte solution. Figure 5 depicts the average velocity as a function of the current for a saline solution when B=0.02 T, L=80 mm, W=2.88 mm, and H=7 mm. The line and symbols in Fig. 5 represent, respectively, the prediction

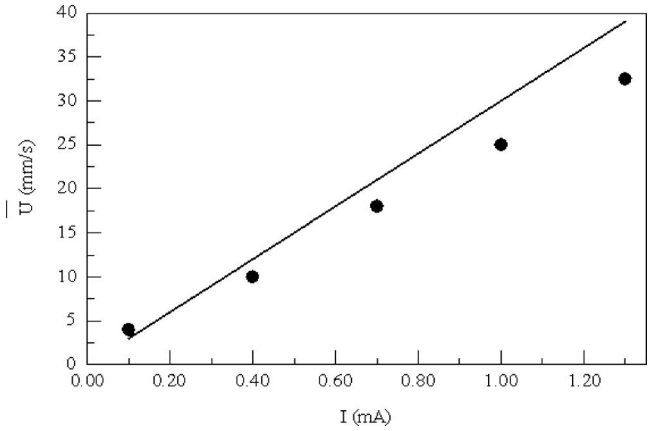

FIG. 5. The average velocity as a function of the externally applied current for a saline solution when $B=0.02$ T, $L=80$ mm, $W=2.88$ mm, and $H=7$ mm. The line and symbols represent, respectively, the prediction of the closed form approximation and the experimental data obtained from the literature.

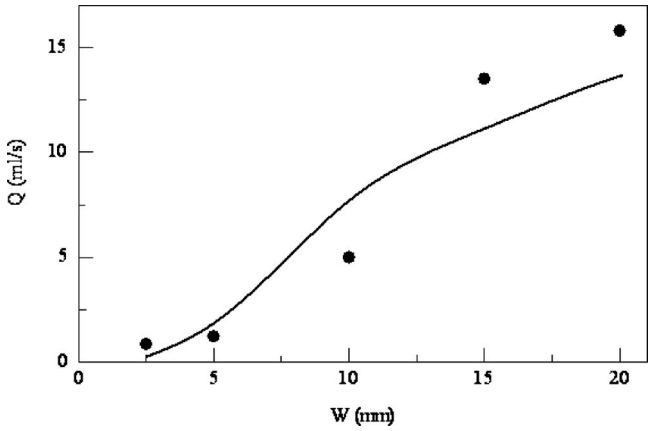

FIG. 6. The flow rate as a function of the width of the channel for a saline solution when $B=0.02$ T, $L=80$ mm, $H=7$ mm, and the externally applied current $I=0.7$ A. The line and symbols represent, respectively, the prediction of the closed form approximation and the experimental data obtained from the literature.

of the closed form approximation (29) and the experimental data obtained from Ho.[13] The predictions from the closed form approximation agree with the experimental data when the current is low. The deviation between the prediction and the experimental data increases as the current increases. In the experiments, since there is no RedOx species present in the solution, there are significant bubble formations under high current conditions. The formed bubbles slow down the fluid motion which explains our predictions are higher than the experimental data when the current is high. Figure 6 depicts the flow rate as a function of the width of the channel for a saline solution when $B=0.02$ T, $L=80$ mm, $H=7$ mm, and the current $I=0.7$ A. The line and symbols represent, respectively, the predictions of the closed form approximation (29) and the experimental data obtained from Ho,[13] and they are in agreement. Therefore, when the currents are prescribed in the experiments, one can estimate the average velocity of the MHD flow with the closed form approximation (28), which shows that the average velocity is linearly proportional to the magnetic flux density B and the current I, and is inversely proportional to the viscosity of the RedOx electrolyte solution. When the potential difference, ΔV, instead of the current is prescribed, the closed form approximation (28) is still valid. However, one first needs to obtain the relationship between the resulting current (I) and the externally applied potential difference (ΔV). Unfortunately, the resulting current depends on many factors such as the configurations of the channel and the electrodes, the characteristics of the electrolyte solution, and the applied voltage. So far, the relationship between them is still not available.

The closed form approximation (28) can also be used to optimize the channel's dimensions and to determine the currents needed to achieve the desired flow patterns and flow rates in complex MHD networks. Figure 7 depicts the average velocity as functions of the height and width of the conduit when its length $L=18$ mm, the magnetic flux density $B=0.44$ T, the current $I=0.15$ mA, and $\Delta p=0$. When the channel is very shallow, the average velocity increases with the width of the channel. This, however, is not true for a wider channel. Once the width exceeds a certain value, the average velocity peaks and then declines with the increase in the channel's width. For a deep channel, the average velocity increases with the width of the channel. When the area of the cross section in the y-z plane and the length of the channel are fixed, there are optimal values for the height and width of the channel under which the flow rate is the maximum. Using the closed form approximation (29) when $\Delta p=0$, the optimal height of the channel derived from $d\bar{U}/dH=0$ is governed by the solution of the following equation:

$$1.5H^6/A^3 + 5.7H^4/A^2 - 1.9A^{1.4}/H^{2.8} - 2.7 = 0, \qquad (30)$$

where A is the area of the cross section in the y-z plane of the channel. The optimal width of the channel is then $W=A/H$. Figure 8 depicts the flow rate $Q=\bar{U}A$, as a function of the height of the channel when the cross-sectional area $A=0.2211$ mm^2, and all other conditions are the same as those in Fig. 7. The predefined cross-sectional area and length are the same as those of the channel used in the experiments by Aguilar *et al.*[25] When the channel is shallow, the flow rate increases as the height increases. When the height of the channel is larger than a threshold value, the flow rate reaches the maximum and then declines with the height. The maximum flow rate occurs in a channel with $H \approx 410$ μm, which corresponds to the solution of Eq. (30).

To further validate the 3D approximation model using the velocity profile (25), Figure 9 depicts the resulting current as a function of the applied potential difference across the two opposing electrodes for the RedOx species $K_4[Fe(CN)_6]$ and $K_3[Fe(CN)_6]$ with concentrations $C_0=0.05$, 0.1, and 0.25 M. The lines and symbols represent, respectively, the solutions of the full 3D mathematical model and the 3D approximation model using the predefined velocity profile (25) without solving the continuity and Navier-Stokes equations. The other conditions are the same as those in Fig. 2. The results from both models are in good agreement, which makes us more confident in applying the 3D approximation model. The resulting current increases as the

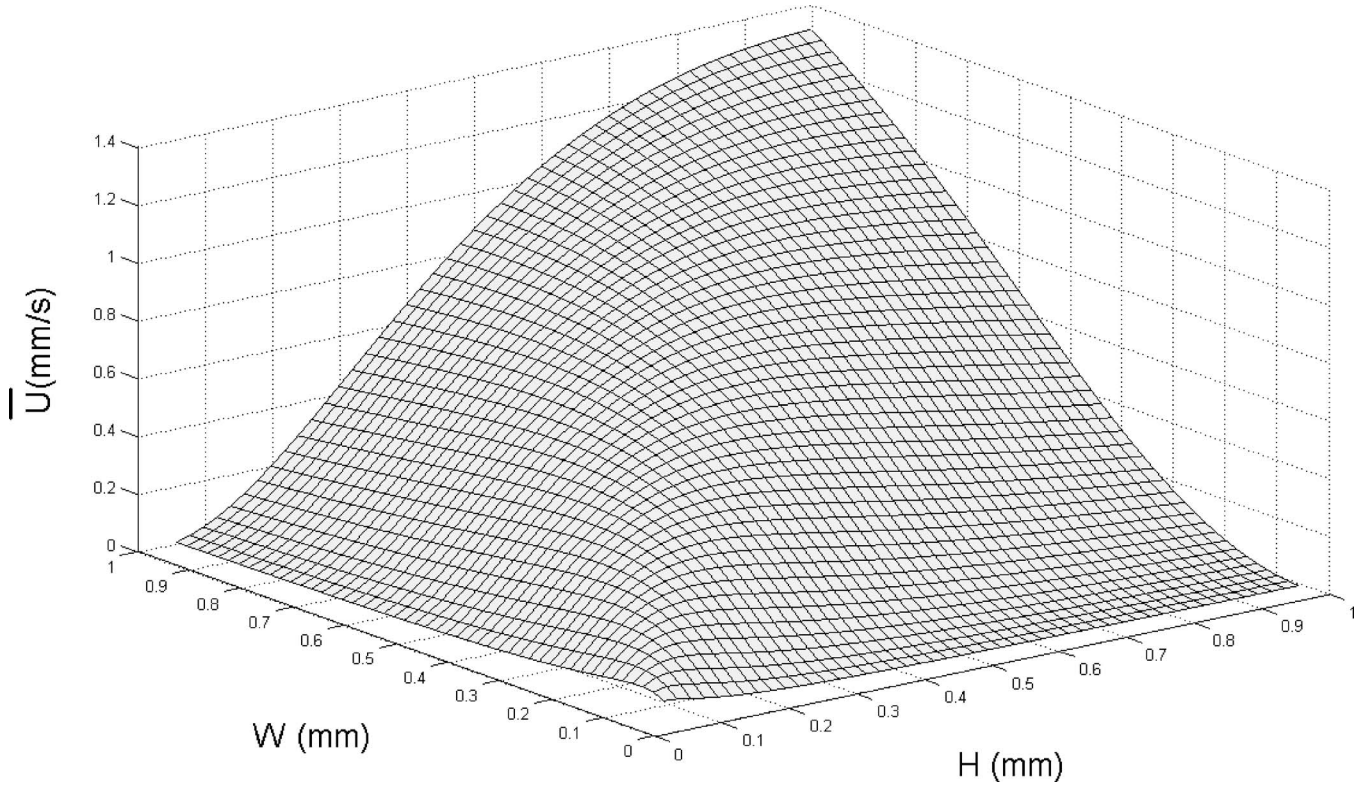

FIG. 7. The average velocity as functions of the height and width of the microchannel with magnetic flux density $B=0.44$ T, applied current $I=0.15$ mA, and length of the conduit $L=18$ mm.

bulk concentration of the RedOx species increases. Next, we check the relationship between the resulting average velocity $\bar{U}$ and the resulting current for various concentrations of the RedOx species under different potential differences. Figure 10 depicts the resulting average velocity $\bar{U}$ as a function of the resulting current for various concentrations of the RedOx species. The resulting currents (x axis) in Fig. 10 are the currents obtained from the full 3D model under various voltages and RedOx concentrations as shown in Fig. 9. The symbols (♦), (▲), and (●) in Fig. 10 represent the resulting average velocities and currents obtained from the full 3D mathematical model for the RedOx species $K_4[Fe(CN)_6]$ and $K_3[Fe(CN)_6]$ with the concentrations $C_0=0.05$, 0.1, and 0.25 M when the applied voltages vary from 0 to 0.4 V. All other conditions are the same as those in Fig. 9. The solid line in Fig. 10 represents the prediction obtained from the

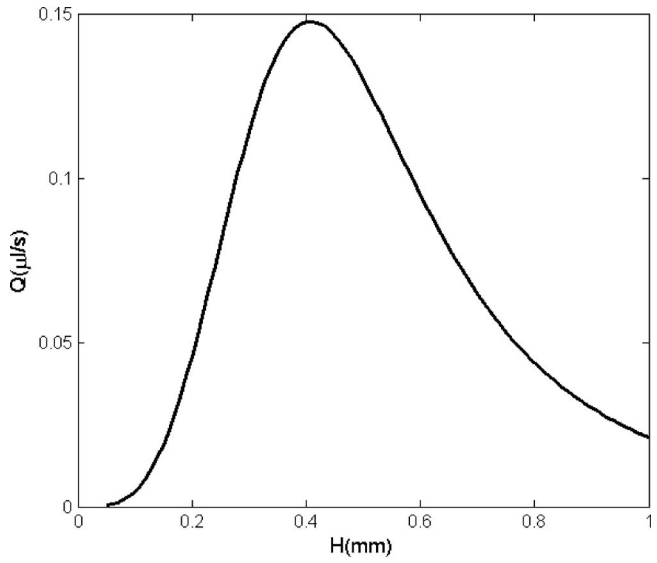

FIG. 8. The flow rate as a function of the height of the microchannel when the magnetic flux density $B=0.44$ T, the applied current $I=0.15$ mA, the length of the conduit $L=18$ mm, and the cross-sectional area in the y-z plane is 0.2211 mm^2.

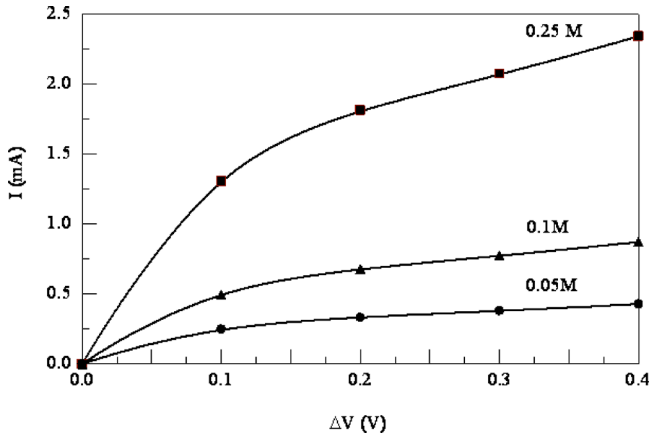

FIG. 9. The resulting current as a function of the externally applied potential difference for various concentrations of the RedOx species $K_4[Fe(CN)_6]/K_3[Fe(CN)_6]$. The lines and symbols represent, respectively, the predictions obtained from the full 3D model and from the 3D approximation model using the predefined velocity profile. All other conditions are the same as Fig. 2.

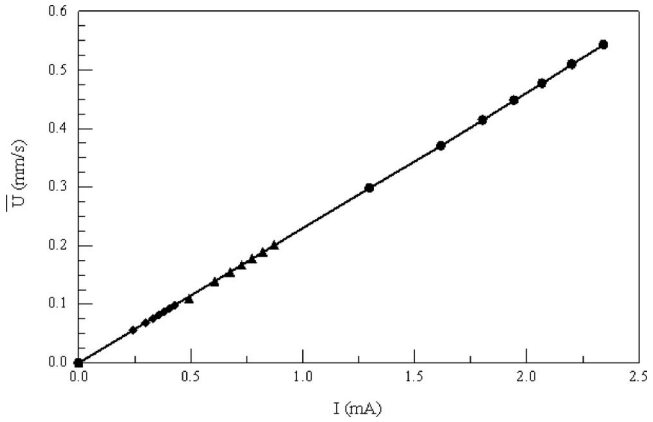

FIG. 10. The average velocity as a function of the resulting current for the RedOx species $K_4[Fe(CN)_6]/K_3[Fe(CN)_6]$ with concentrations C_0=0.05 M (♦), 0.1 M (▲), and 0.25 M (●). The symbols and solid line represent, respectively, the predictions obtained from the full 3D model and from the closed form approximation. All other conditions are the same as Fig. 2.

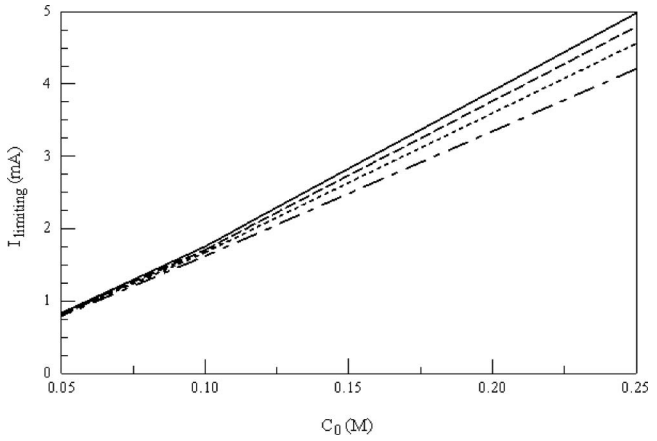

FIG. 11. The limiting current as a function of the concentration of the RedOx species $K_4[Fe(CN)_6]/K_3[Fe(CN)_6]$. The solid, dashed, dotted, and dash-dotted lines represent, respectively, the limiting currents when the magnetic flux densities are B=0.8 T, 0.6 T, 0.44 T, and 0.2 T. All other conditions are the same as Fig. 2.

closed form approximation (29). It is clearly shown that resulting average velocity $\bar{U}$ is linearly proportional to the resulting current I for various concentrations of the RedOx species and different applied voltages. The predictions obtained from the full 3D mathematical model (symbols in Fig. 10) agree favorably with those obtained from the closed form approximation (solid line).

Since the average velocity or flow rate is proportional to the resulting current, the average velocity or flow rate reaches the maximum under the limiting current condition under which the concentrations of the Ox ions at the surface of the cathode and the Red ions at the surface of the anode equal zero, and the resulting current does not change with the externally applied voltage. As $U_{an}=-U_{ca}=\Delta V/2$ and $\Delta V\rightarrow\infty$, the current tends to the limiting current with $c_{Red}=0$ at the surface of the anode and $c_{Ox}=0$ on the surface of the cathode. The limit current provides the upper bound on the average velocity (flow rate) of the MHD flow. In the numerical simulations, we chose ΔV=2 V under which the conditions $c_{Red}=0$ on the anode and $c_{Ox}=0$ on the cathode were satisfied, and the resulting currents correspond to the limiting currents. Figure 11 depicts the limiting current $I_{limiting}$ as a function of the concentrations of the RedOx species $K_4[Fe(CN)_6]$ and $K_3[Fe(CN)_6]$ under various magnetic flux densities. The dimensions of the channel are the same as those in Fig. 2. The results in Fig. 11 are obtained from the full 3D mathematical model. The dash-dotted, dotted, dashed, and solid lines represent, respectively, the limiting currents at B=0.2, 0.44, 0.6, and 0.8 T. The limiting current increases nearly linearly with the RedOx concentration under various magnetic flux densities. The linear relationship between the limiting current and the bulk concentration of the RedOx species agree with the experimental observations by Arumugam *et al.*[26] Figure 12 depicts the maximum average velocity corresponding to the limiting current condition as a function of the bulk concentration of the RedOx species. The lines and symbols in Fig. 12 represent, respectively, the predictions obtained from the full 3D mathematical model and from the closed form approximation (29) using the obtained resulting current as depicted in Fig. 11. Once again, the predictions from the closed form approximation agree well with those obtained from the full 3D mathematical model. Due to the linear relationship between the average velocity and the resulting current whose limiting value is linearly proportional to the bulk concentration of the RedOx species, the maximum average velocity $\bar{U}_{max}$ is also linearly proportional to the bulk concentration of the RedOx species present in the electrolyte solution. The results imply that one can enhance the flow by using higher concentration of the RedOx species. However, the presence of concentrated RedOx species may damage some targets such as DNA and enzyme present in some biological applications.

Finally, to shed light on the effect of the magnetic flux density B on the limiting current ($I_{limiting}$), Fig. 13 depicts the limiting current as a function of the magnetic flux density for

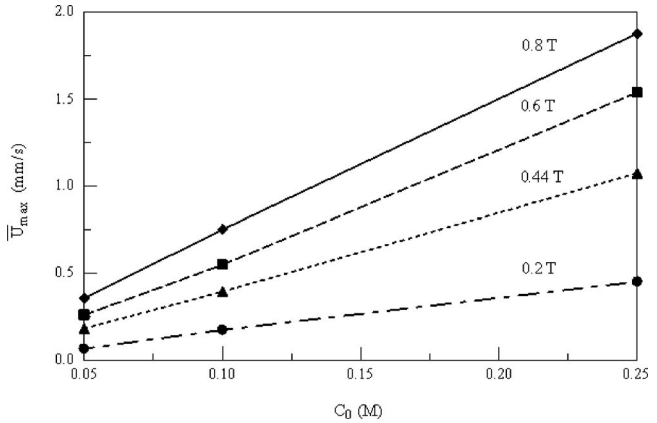

FIG. 12. The average velocity under the limiting current condition as a function of the concentration of the RedOx species $K_4[Fe(CN)_6]/K_3[Fe(CN)_6]$ under various magnetic flux densities. The lines and symbols represent, respectively, the results obtained from the full 3D model and from the closed form approximation using the values of the limiting current as depicted in Fig. 11. All other conditions are the same as Fig. 2.

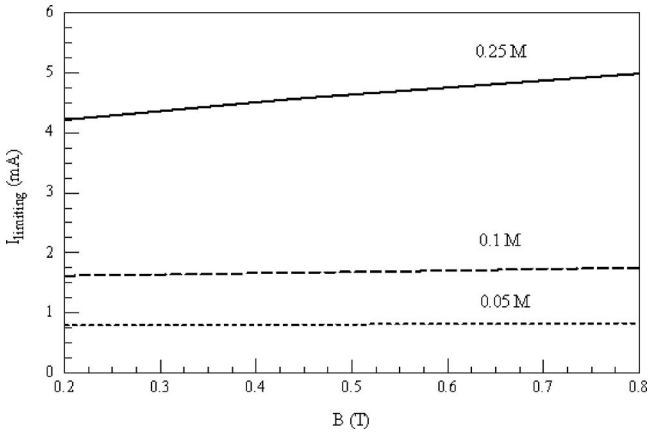

FIG. 13. The limiting current as a function of the magnetic flux density for various concentrations of the RedOx species $K_4[Fe(CN)_6]/K_3[Fe(CN)_6]$. All other conditions are the same as Fig. 2.

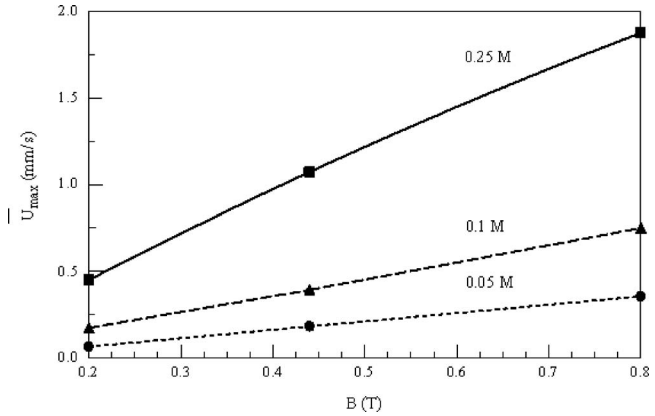

FIG. 14. The average velocity corresponding to the limiting current as a function of the magnetic flux density under various concentrations of the RedOx species $K_4[Fe(CN)_6]/K_3[Fe(CN)_6]$. The lines and symbols represent, respectively, the predictions obtained from the full mathematical model and from the closed form approximation using the values of the limiting current as depicted in Fig. 13. All other conditions are the same as Fig. 2.

the RedOx species with concentrations $C_0=0.05$ M (dotted line), 0.1 M (dashed line), and 0.25 M (solid line). When the concentration of the RedOx species is low, the limiting current is nearly independent of the magnetic flux density. As the concentration of the RedOx species increases, so does the effect of the magnetic flux density on the limiting current. For higher concentration of the RedOx species, the limiting current increases nearly linearly with the magnetic flux density. As the magnetic flux density increases, the induced MHD flow increases, the thicknesses of the concentration boundary layers next to the electrodes decrease. Consequently, the current density and the total current increase. Figure 14 depicts the maximum average velocity corresponding to the limiting current condition as a function of the magnetic flux density under various concentrations of the RedOx species. The conditions are the same as those in Fig. 13. According to the expression (29), the effect of the magnetic flux density on the average velocity is due to the combined effects of B on the current and B itself. For low concentration of the RedOx species, since the effect of the magnetic flux density on the limiting current is insignificant (Fig. 13), the average velocity under the limiting current condition linearly increases as the magnetic flux density increases. For higher concentration of the RedOx species, the effects of the magnetic flux density on the limiting current also come into play. The theoretical predictions from the full 3D mathematical model (lines) agree well with the predictions obtained from the closed form approximation (symbols) using the obtained limiting current as depicted in Fig. 13.

V. CONCLUSIONS

We introduced a full 3D mathematical model consisting of the coupled Nernst-Planck equations for the concentration fields of the ionic species in solution, the generalized Butler-Volmer equation for the electron transfer, and the Navier-Stokes equations for the flow field to investigate the performance of RedOx-based MHD microfluidic devices under various operating conditions. The model presented here will be useful for the design and optimization of RedOx-based MHD microfluidic devices. Moreover, the model allows one to test rapidly and inexpensively the effects of various parameters and operating conditions on the device's performances. The major conclusions are:

(i) The resulting current transmitted through the electrolyte solution increases nonlinearly with the externally applied potential difference. The theoretical predictions obtained from the 3D mathematical model agree with the experimental data obtained from the literature. However, the 2D model overpredicts the current and the average velocity (flow rate) since the effects of the top and bottom dielectric walls on the flow and mass transport have not been taken into account.

(ii) In planar microconduits, a 3D approximation model was introduced where the velocity profile is approximated by that of a fully developed duct flow with a rectangular cross section. Upon doing so, one only needs to solve the Nernst-Planck and the local electroneutrality equations without solving the continuity and Navier-Stokes equations. The results obtained from the full 3D model and from the 3D approximation model are in excellent agreement.

(iii) A closed form approximation for the average velocity (flow rate) was derived in terms of the current, applied pressure difference, the strength of the magnetic flux density, viscosity of the fluid, and the dimensions of the channel. The average velocities obtained from the full 3D model, the 3D approximation model, and the closed form approximation are in good agreement and qualitatively agree with the experimental observations obtained from the literature. The closed form approximation can be used to optimize the dimensions of the channel and to solve the control (inverse) problems in MHD networks so as to achieve the desired flow patterns and flow rates.

(iv) The average velocity (flow rate) linearly increases with the increase in the current for different concen-

trations of the RedOx species, various magnetic flux densities, and dimensions of the channel.

(v) The limiting current and the average velocity (flow rate) under the limiting current condition linearly increase with the concentration of the RedOx species under various magnetic flux densities.

(vi) When the concentration of RedOx species is low, the effects of the magnetic flux density on the limiting current are negligible. For higher concentration of the RedOx species, the limiting current increases with the magnetic flux density. Under the limiting current condition, the average velocity (flow rate) almost linearly increases with the magnetic flux density under various concentrations of the RedOx species.

ACKNOWLEDGMENTS

One of the authors (S.Q.) acknowledges partial support from the National Science Foundation under Grant No. 0447416 and UNLV NIA grant. We also acknowledge Mr. Juan K. Afonien and Mr. Martin Mack for their valuable help.

[1] J. Jang and S. S. Lee, "Theoretical and experimental study of MHD (Magnetohydrodynamic) micropump," Sens. Actuators, A **80**, 84 (2000).
[2] A. V. Lemoff and A. P. Lee, "An AC magnetohydrodynamic micropump," Sens. Actuators B **63**, 178 (2000).
[3] H. H. Bau, "A case for magneto-hydrodynamics (MHD)," in Proceedings of ASME International Mechanical Engineering Congress and Exposition, New York, NY, Nov. 11–16, 2001, Paper No. 23884.
[4] J. H. Zhong, M. Yi, and H. H. Bau, "Magneto hydrodynamic (MHD) pump fabricated with ceramic tapes," Sens. Actuators, A **96**, 59 (2002).
[5] H. H. Bau, J. Zhu, S. Qian, and Y. Xiang, "A magneto-hydrodynamic (MHD) micro fluidic network," in Proceedings of ASME International Mechanical Engineering Congress and Exposition, New Orleans, LA, Nov. 17–22, 2002, Paper No. 33559.
[6] H. H. Bau, J. Zhu, S. Qian, and Y. Xiang, "A magneto-hydrodynamically controlled fluidic network," Sens. Actuators B **88**, 205 (2003).
[7] J. West, J. P. Gleeson, J. Alderman, J. K. Collins, and H. Berney, "Structuring laminar flows using annular magnetohydrodynamic actuation," Sens. Actuators B **96**, 190 (2003).
[8] A. Homsy, S. Koster, J. C. T. Eijkel, A. van den Berg, F. Lucklum, E. Verpoorte, and N. F. de Rooij, "A high current density DC magnetohydrodynamic (MHD) micropump," Lab Chip **5**, 466 (2005).
[9] J. C. T. Eijkel, A. Van den Berg, and A. Manz, "Cyclic electrophoretic and chromatographic separation methods," Electrophoresis **25**, 243 (2004).
[10] E. Sawaya, N. Ghaddar, and F. Chaaban, "Evaluation of the hall parameter of electrolyte solutions in thermosyphonic MHD flow," Int. J. Eng. Sci. **40**, 2041 (2002).
[11] N. Ghaddar and E. Sawaya, "Testing and modeling thermosyphonic closed-loop magnetohydrodynamic electrolyte flow," J. Thermophys. Heat Transfer **17**, 129 (2003).
[12] J. West, B. Karamata, B. Lillis, J. P. Gleeson, J. Alderman, J. K. Collins, W. Lane, A. Mathewson, and H. Berney, "Application of magnetohydrodynamic actuation to continuous flow chemistry," Lab Chip **2**, 224 (2002).
[13] J. Ho, "Study the performance of MHD pump with the dimension of duct channel," Journal of Marine Science and Technology (in press, 2007).
[14] H. H. Bau, J. Zhong, and M. Yi, "A minute magnetohydrodynamic (MHD) mixer," Sens. Actuators B **79**, 205 (2001).
[15] M. Yi, S. Qian, and H. H. Bau, "A magnetohydrodynamic chaotic stirrer," J. Fluid Mech. **468**, 153 (2002).
[16] S. Qian, J. Zhu, and H. H. Bau, "A stirrer for magnetohydrodynamically controlled minute fluidic networks," Phys. Fluids **14**, 3584 (2002).
[17] Y. Xiang and H. H. Bau, "Complex magnetohydrodynamic low-Reynolds-number flows," Phys. Rev. E **68**, 016312 (2003).
[18] J. P. Gleeson, O. M. Roche, J. West, and A. Gelb, "Modeling annular micromixers," SIAM J. Appl. Math. **64**, 1294 (2004).
[19] S. Qian and H. H. Bau, "Magnetohydrodynamic stirrer for stationary and moving fluids," Sens. Actuators B **106**, 859 (2005).
[20] E. A. Clark and I. Fritsch, "Anodic stripping voltammetry enhancement by RedOx magnetohydrodynamics," Anal. Chem. **76**, 2415 (2004).
[21] P. U. Arumugam, A. J. Belle, and I. Fritsch, "Inducing convection in solutions on a small scale: Electrochemistry at microelectrodes embedded in permanent magnets," IEEE Trans. Magn. **40**, 3063 (2004).
[22] P. U. Arumugam, E. A. Clark, and I. Fritsch, "Use of paired, bonded NdFeB magnets in RedOx magnetohydrodynamics," Anal. Chem. **77**, 1167 (2005).
[23] S. Qian and H. H. Bau, "Magneto-hydrodynamic flow of RedOx electrolyte," Phys. Fluids **17**, 067105 (2005).
[24] E. C. Anderson and I. Fritsch, "Factors influencing RedOx magnetohydrodynamic-induced convection for enhancement of stripping analysis," Anal. Chem. **78**, 3745 (2006).
[25] Z. Aguilar, P. Arumugam, and I. Fritsch, "Study of magnetohydrodynamic driven flow through LTCC channel with self-contained electrodes," J. Electroanal. Chem. **591**, 201 (2006).
[26] P. Arumugam, E. Fakunle, E. Anderson, S. Evans, K. King, Z. Aguilar, C. Carter, and I. Fritsch, "Characterization and pumping RedOx magnetohydrodynamics in a microfluidic channel," J. Electrochem. Soc. **153**, E185 (2006).
[27] S. Qian, Z. Chen, J. Wang, and H. H. Bau, "Electrochemical reaction with RedOx electrolyte in toroidal conduits in the presence of natural convection," Int. J. Heat Mass Transfer **49**, 3968 (2006).
[28] S. R. Ragsdale, K. M. Grant, and H. S. White, "Electrochemically generated magnetic forces. Enhanced transport of a paramagnetic RedOx species in large, nonuniform magnetic fields," J. Am. Chem. Soc. **120**, 13461 (1998).
[29] J. Newman, *Electrochemical Systems*, 2nd ed. (Prentice-Hall, Englewood Cliffs, NJ, 1991).
[30] A. J. Bard and L. R. Faulkner, *Electrochemical Methods, Fundamentals and Applications*, 2nd ed. (John Wiley and Sons, Englewood Cliffs, NJ, 2000).
[31] S. Qian and J. F. L. Duval, "Modulation of electroosmotic flows in electron-conducting microchannels by coupled quasi-reversible faradaic and adsorption-mediated depolarization," J. Colloid Interface Sci. **300**, 413 (2006).
[32] M. Georgiadou, "Modeling current density distribution in electrochemical systems," Electrochim. Acta **48**, 4089 (2003).
[33] Y. Marcus, *Ion Properties* (Marcel Dekker, New York, 1997).
[34] L. Bortels, B. Van den Bossche, J. Deconinck, S. Vandeputte, and A. Hubin, "Analytical solution for the steady-state diffusion and migration involving multiple reacting ions: Application to the identification of Butler-Volmer kinetic parameters for the ferri-/ferrocyanide RedOx couple," J. Electroanal. Chem. **429**, 139 (1997).
[35] F. M. White, *Viscous Fluid Flow*, 3rd ed. (McGraw-Hill, New York, 2006).
[36] N. Natarajan and S. M. Lakshmanan, "Laminar flow in rectangular ducts: prediction of velocity profiles and friction factor," Indian J. Technol. **10**, 435 (1972).